

Resolved Spectroscopy of the Narrow-Line Region in NGC 1068.

I. The Nature of the Continuum Emission¹

D. Michael Crenshaw² & Steven B. Kraemer³

Catholic University of America and Laboratory for Astronomy and Solar Physics, NASA's
Goddard Space Flight Center, Code 681, Greenbelt, MD 20771

Received _____; accepted _____

¹Based on observations with the NASA/ESA *Hubble Space Telescope*, which is operated by the Association of Universities for Research in Astronomy, Inc., under NASA contract NAS5-26555.

²crenshaw@buckeye.gsfc.nasa.gov

³stiskraemer@yancey.gsfc.nasa.gov

ABSTRACT

We present the first long-slit spectra of the Seyfert 2 galaxy NGC 1068 obtained by the Space Telescope Imaging Spectrograph (STIS); the spectra cover the wavelength range 1150 – 10,270 Å at a spatial resolution of 0".05 – 0".1 and a spectral resolving power of $\lambda/\Delta\lambda \approx 1000$. In this first paper, we concentrate on the far-UV to near-IR continuum emission from the continuum “hot spot” and surrounding regions extending out to $\pm 6".0$ (± 432 pc) at a position angle of 202° .

In addition to the broad emission lines detected by spectropolarimetry, the hot spot shows the “little blue bump” in the 2000 – 4000 Å range, which is due to Fe II and Balmer continuum emission. The continuum shape of the hot spot is indistinguishable from that of NGC 4151 and other Seyfert 1 galaxies. Thus, the hot spot is reflected emission from the hidden nucleus, due to electron scattering (as opposed to wavelength-dependent dust scattering). The hot spot is $\sim 0".3$ in extent and accounts for 20% of the scattered light in the inner 500 pc.

We are able to deconvolve the extended continuum emission in this region into two components: electron-scattered light from the hidden nucleus (which dominates in the UV) and stellar light (which dominates in the optical and near-IR). The scattered light is heavily concentrated towards the hot spot, is stronger in the northeast, and is enhanced in regions of strong narrow-line emission. The stellar component is more extended, concentrated southwest of the hot spot, dominated by an old ($\geq 2 \times 10^9$ years) stellar population, and includes a nuclear stellar cluster which is ~ 200 pc in extent.

Subject headings: galaxies: individual (NGC 1068) – galaxies: Seyfert

1. Introduction

NGC 1068 is the nearest and brightest Seyfert 2 galaxy, and has been the subject of intense scrutiny over the entire electromagnetic spectrum (including a recent workshop devoted entirely to this object, see Gallimore & Tacconi 1997). The detection of broad (FWHM $\approx 4500 \text{ km s}^{-1}$) emission lines in the polarized flux from NGC 1068 (Antonucci & Miller 1985; Miller, Goodrich, & Mathews 1991) revealed a Seyfert 1 nucleus (characterized by broad lines and a strong nonstellar continuum) that is hidden from our direct line of sight, but can be seen in reflected light due to electron and/or dust scattering in the circumnuclear regions. Thus, NGC 1068 formed the basis of unified models for Seyfert galaxies, which postulate that Seyfert 1 and 2 galaxies are basically the same type of object, but viewed from different angles relative to the source of obscuration (e.g., an optically thick torus, see Antonucci 1993).

Ground-based images of the outer narrow-line region (NLR), obtained in narrow wavebands centered on strong emission lines (Pogge 1988), have revealed a cone-like structure along the radio axis (which can also be explained by a thick torus). Subsequent observations with the *Hubble Space Telescope* (HST) at high spatial resolution ($\sim 0''.1$) have shown that the inner NLR contains numerous knots and filaments, also in a cone-like geometry (Evans et al. 1991; Macchetto et al. 1994) with an apparent opening angle of $65^\circ \pm 25^\circ$ and a position angle on the sky of $\text{PA} \approx 15^\circ$ (whereas the outer NLR has $\text{PA} \approx 30 - 35^\circ$). These authors admit that the apex of the cone is difficult to determine and seems to change with contrast level, but lies within $\sim 0''.4$ of the continuum peak.

HST images of the optical continuum emission from the NLR show a bright, resolved peak of emission, which has been named the “continuum hot spot”. The hot spot is $\sim 0''.3$ in size and is surrounded by an extended structure that is elongated in the NE-SW direction, has approximate dimensions of $3''.5 \times 1''.7$, and is centered about $0''.4$ SW of the hot spot.

Lynds et al. (1991) suggest that this extended region is dominated by stellar light, but that polimetry and/or spectroscopy are needed for verification. By contrast, HST images of the UV continuum emission resemble those of the emission lines, and in particular, show that the hot spot and a conical region NE of it are bright in the UV (Kriss et al. 1993; Macchetto et al. 1994).

Numerous spectra of NGC 1068 have been taken from the ground (e.g., see Koski 1978), and a high-quality UV spectrum obtained with *IUE* is shown in Snijders, Netzer, & Boksenberg (1986). Caganoff et al. (1991) give the first *HST* spectrum, which was obtained by the Faint Object Spectrograph (FOS) through a $0''.3$ diameter aperture centered on the continuum hot spot, and covers the wavelength region $2200 - 7000 \text{ \AA}$. These authors suggest that the hot spot is *not* the source of reflected light from the hidden nucleus, because they were unable to detect broad $H\beta$ at the large velocity width and equivalent width seen in optical spectropolarimetry. However, Antonucci, Hurt, & Miller (1994) present *HST* UV ($1575 - 3300 \text{ \AA}$) spectropolarimetry of the hot spot (see also Code et al. 1993), and show that the highly polarized ($\sim 20\%$) light within the $0''.3$ aperture shows broad C III] and Mg II emission, as well as blended Fe II emission, indicating that at least some of the light from the hot spot is reflected emission from the hidden broad-line region (BLR). Antonucci et al. (1994) also find that the scattering region is extended over at least $\sim 1''$, and is dominated by electron scattering on this spatial scale, since the polarization does not change as a function of wavelength.

Other FOS observations have been obtained at various locations in the NLR, and we have compared these observations with detailed photoionization models to study the physical conditions in these regions (Kraemer, Ruiz, & Crenshaw 1998). However, these observations were obtained prior to the installation of COSTAR, and the regions sampled contained large contributions from outside the $0''.3$ aperture used. Clearly, observations

at spatial resolutions comparable to that of the HST images ($\sim 0''.1$) are important for understanding the nature of the hot spot, as well as the detailed structure and kinematics of the NLR in NGC 1068. The Space Telescope Imaging Spectrograph (STIS) is an ideal instrument for this purpose, since it provides long-slit capability at high spatial resolution in the UV, optical, and near-IR.

In this paper, we describe our STIS observations of NGC 1068, and investigate the nature of the continuum emission, including the hot spot and its surroundings. In subsequent papers, we give results on the compact high-ionization region, the detailed kinematics of the emission-line clouds, and the physical conditions and reddening across the NLR. We adopt a systemic redshift of $cz = 1148 \text{ km s}^{-1}$ from H I observations (Brinks et al. 1997) and a distance of 14.4 Mpc (Bland-Hawthorne 1997), so that $0''.1$ corresponds to 7.2 pc.

2. Observations and Data Reduction

We observed NGC 1068 with *HST*/STIS on 1998 August 15. We used the $52'' \times 0''.1$ slit to obtain low-dispersion spectra over the wavelength range $1150 - 10,270 \text{ \AA}$ at a spectral resolving power of $\lambda/\Delta\lambda \approx 1000$ and spatial resolution of $0''.1$ (CCD detector) or $0''.05$ (MAMA detectors, which only contain $25''$ of the slit length). Table 1 gives the grating, detector, wavelength coverage, and total exposure time for each setting.

Our slit position was chosen to intersect a number of bright emission-line knots in the inner NLR. Figure 1 shows the slit position, at $PA = 202^\circ$, superimposed on an FOC [O III] image (Macchetto et al. 1994). Our procedure for positioning the slit was to perform an extended-source target acquisition with STIS on the hot spot (using the continuum centroid in a $0''.35 \times 0''.35$ box), and offset the center of the slit to a position $0''.14$ north of the

continuum peak. This position places emission knot C in the center of the slit, and includes knots B and D (using the nomenclature of Evans et al. 1991); for the purpose of discussion, we identify two additional knots in Figure 1 as “H” and “I”. Figure 2 shows our slit position superimposed on a WFPC2 continuum image centered at 5470 Å. From this image, one can see that the slit includes a significant portion of the hot spot, offset from its center.

We reduced the STIS data using the IDL software developed at NASA’s Goddard Space Flight Center for the Instrument Definition Team. We identified and removed cosmic ray hits using the multiple images obtained in each mode, and removed hot or warm pixels (identified in STIS dark images) by interpolating over them in the dispersion direction. We used wavelength calibration exposures obtained after each science observation to correct the wavelength scale for zero-point shifts. In order to correct for the high instrumental background of the near-UV MAMA (Kimble et al. 1998), we determined a background spectrum (in counts/sec) by median filtering and averaging 100 rows near the top of the G230L spectral image (at a projected location $9''.5 - 12''.0$ southwest of the hot spot), and subtracted this background from each row in the image. We performed the same procedure for the other spectral images, although this had little effect, since the background counts for these detectors were much lower. Finally, we used the “extended” option in our reductions, which geometrically rectifies the spectral images to produce a constant wavelength along each column (in the spatial direction), and fluxes at each position along the slit in units of $\text{ergs s}^{-1} \text{ cm}^{-2} \text{ \AA}^{-1}$ per cross-dispersion pixel (fluxes are conserved in the geometric transformations).

We show the flux-calibrated images for the G140L and G430L observations in Figures 3 and 4; note that the top of these images corresponds to the lower right-hand (SW) area in Figures 1 and 2. The images show both smooth and discrete structure in the spatial distribution of continuum and emission-line fluxes, which appear to coincide in many

locations. (The emission lines show complex kinematic structure, which will be the topic of another paper.) The continuum hot spot is very prominent in both images, and we will use it as a reference location. The prominent continuum streak below the hot spot is knot “H”, and the one above is “I”. One interesting aspect of these images is that the extended UV continuum is concentrated below the hot spot (NE) in Figure 3, whereas the optical continuum is concentrated above the hot spot (SW) in Figure 4.

To obtain spectra at different spatial locations, we used the extraction bins shown in Figures 1 and 2. We found that a bin length of $0''.2$ (4 CCD pixels, 8 MAMA pixels) yields reasonable signal-to-noise ratios in the continuum, and is sufficient to isolate the extended continuum and emission-line structure. We extracted spectra from each bin to a distance of $\pm 6''$ from the hot spot, and, at each position, combined spectra from different gratings in their regions of overlap. The central $0''.2 \times 0''.1$ bin contains the portion of the hot spot that was intercepted by the slit.

3. Results

3.1. Scattered Broad-Line Emission from the Hot Spot

In Figure 5, we compare the entire UV to near-IR spectrum of the hot spot with a STIS spectrum of the nucleus of NGC 4151, obtained over the same wavelength region (from Nelson et al. 1999, reduced in flux by a factor of 0.015). The overall continuum shapes are remarkably similar, and both spectra show a “little blue bump” in the 2000 - 4000 Å region. The blue end (2200 Å – 3200 Å) of this feature was detected in NGC 1068 by *IUE* (Snijders et al. 1986), and confirmed with FOS spectra (Antonucci et al. 1994). These authors attribute the feature to reflected Fe II emission from the hidden nucleus, which is expected from the presence of optical Fe II emission in spectropolarimetry of NGC 1068

(Antonucci & Miller 1985; Miller et al. 1991). Our STIS spectra show that this feature extends to 4000 Å and is the same shape as that in Seyfert 1 galaxies, which confirms its identity as the little blue bump. The presence of significant emission above the continuum at 3200 – 4000 Å indicates that much of this feature is due to Balmer continuum emission, since Fe II contributes little to the bump in this wavelength region (Wills, Netzer, & Wills 1985). The little blue bump is a common feature in the spectra of Seyfert 1 galaxies and QSOs, and can be explained by a combination of Fe II and Balmer continuum emission from dense gas in the BLR (Wills et al. 1985). As can be seen in Figure 5, the strength of the little blue bump in the hot spot spectrum, relative to the continuum, is 1/3 that in the NGC 4151 spectrum. Nevertheless, the presence of this feature in our spectrum clearly identifies the continuum hot spot as a strong reflector of light from the hidden nucleus.

Further evidence for reflected light can be seen in Figure 6, which shows an expanded view of the far-UV spectrum of the hot spot. This spectrum shows narrow emission lines from knot B (which overlaps with the hot spot) and strong absorption lines from our Galaxy, but no evidence for broad stellar absorption features like those seen in the N V and Si IV lines of the Seyfert 2 galaxy Mrk 477, which indicate the presence of hot young stars in this object (Heckman et al. 1997). However, broad components are clearly seen in the $L\alpha$ and C IV λ 1550 emission lines (which were first detected in the *IUE* spectrum of Snijders et al. 1986), indicating reflected radiation from the hidden nucleus. The broad component of C IV is the easiest to isolate, and is characterized by a velocity width (FWHM) = 5200 ± 800 km s⁻¹ and an equivalent width (EW) = 23 ± 2 Å. The velocity width is in the middle of the range for Seyfert 1 galaxies, whereas the EW is definitely on the low side, but not outside of the Seyfert 1 range (see Kinney et al. 1990).

Our detection of the little blue bump and broad components of the far-UV emission lines confirms Antonucci et al.’s (1994) finding, from near-UV (1600 – 3300 Å) spectropolarimetry,

that the hot spot reflects emission from the hidden BLR. We can also compare our optical spectra with those obtained through a $0''.3$ diameter aperture with the FOS (Caganoff et al. 1991), and with ground-based spectropolarimetry through a $2''$ -wide slit (Miller et al. 1991). Caganoff et al. (1991) reported that they saw a component of $H\beta$ that has a FWHM of only 2200 km s^{-1} , and concluded that they did *not* detect the broad component of $H\beta$ seen in the polarized spectra of the nucleus, which has a FWHM of 4480 km s^{-1} (Miller et al. 1991). Figure 7 shows our removal of the narrow component of $H\beta$ in the STIS spectrum, using the [O III] $\lambda 5007$ line as a template (note that the velocity width of [O III] is large: $\text{FWHM} = 1180 \text{ km s}^{-1}$). We find that the velocity width of the broad component of $H\beta$ is $\text{FWHM} = 3800 \pm 700 \text{ km s}^{-1}$, which is consistent with Miller et al.’s results, to within the errors.

However, we confirm Caganoff et al.’s measurement of a small equivalent width for broad $H\beta$: our measurements yield $\text{EW}(H\beta) = 25 \pm 5 \text{ \AA}$, compared to Caganoff et al.’s 16 \AA , whereas Miller et al.’s spectropolarimetry yields 110 \AA . As we mentioned earlier, the equivalent widths of C IV and the little blue bump are also low, compared to most Seyfert 1 galaxies, indicating intrinsically weak emission from the BLR. The small equivalent widths in our spectra cannot be due to a large stellar contribution to the continuum, because the hot spot’s continuum emission is dominated by scattered light; since the stellar light contribution is $\leq 31\%$ (see below), the equivalent width of $H\beta$, relative to the nonstellar continuum, cannot be larger than 36 \AA .

Assuming that the starlight has been properly accounted for in the ground-based observations, our results indicate that the equivalent width of broad $H\beta$, relative to the nonstellar continuum, is a function of aperture size. Since the HST spectra are sampling a scattering region that is much smaller ($0''.3$ or 21.6 pc) and closer (on average) to the continuum source than that sampled by ground based-observations, a likely explanation

is that the equivalent width of broad $H\beta$ was actually much lower over a period of ~ 70 years (the light travel time across the hot spot), compared to the previous ~ 700 years. For example, the BLR clouds could be matter-bounded, so that a large increase in luminosity would not result in a significant increase in broad-line emission. Another possibility is that the amount of material in the BLR was much smaller over this time period, resulting in a low covering factor, and hence small equivalent widths.

3.2. The Continuum Emission from the Hot Spot

As we mentioned previously, the far-UV to near-IR continuum of the hot spot in NGC 1068 is very similar to that of Seyfert 1 galaxies. To quantify the similarity, we fit the continuum regions over $1200 - 10,000 \text{ \AA}$ (excluding the little blue bump) with a power law of the form $F_\nu \propto \nu^\alpha$. For the hot spot, we find $\alpha = -0.5 \pm 0.2$, whereas for NGC 4151, we find $\alpha = -0.6 \pm 0.1$. The shape of the hot spot continuum is essentially identical to that of NGC 4151, and similar to that seen in Seyfert 1 galaxies and QSOs (Wills et al. 1985). From this remarkable similarity, we conclude: 1) the continuum emission from the hot spot is dominated by reflected light from the hidden nucleus, since a large stellar contribution would produce a much redder continuum (see below), and 2) the scattering is wavelength independent and must therefore be due to electrons, since dust scattering would produce a much bluer spectrum than generally observed in Seyfert 1 galaxies.

There appears to be a slight turnover in the spectrum of the hot spot at $\lambda < 1450 \text{ \AA}$. Dereddening the spectrum, assuming $E(B-V) = 0.1$ and the standard Galactic reddening curve (Savage & Mathis 1979), eliminates the turnover, but it 1) introduces an artificial emission bump at 2200 \AA , and 2) makes the continuum much harder ($\alpha \approx -0.2$) than typical values for Seyfert 1 galaxies (Wills et al. 1985). In order to avoid an artificial bump at 2200 \AA , the continuum reddening must be $E(B-V) \leq 0.05$, but this upper limit can be

avoided if the bump is not a feature of the reddening curve in this object (Kriss et al. 1992; Antonucci et al. 1994). Another indication of low continuum reddening was found by Kriss et al. (1992) from a power-law plus reddening curve fit to the observed continuum in *HUT* spectra obtained through a large aperture ($18''$), resulting in $E(B-V) = 0.065 \pm 0.02$.

3.3. The Extended Continuum Emission

Figure 8 shows our extracted spectra at four locations along the slit: the hot spot, positions H and I, and a region $3''$ to $6''$ SW of the hot spot (the “galaxy” spectrum). It is clear that the continuum shape varies greatly as a function of position, suggesting the presence of more than one contributor. In order to separate the contributions, we assumed that the continuum at each location consists of two components: 1) scattered-light from the hidden nucleus, which is given by the spectrum of the hot spot, and 2) stellar light from the host galaxy, which is obtained by summing the region $3''$ to $6''$ SW of the hot spot. We then derived templates for the scattered and stellar continua by fitting these two spectra with cubic splines in regions unaffected by emission or absorption (but including the little blue bump in the scattered spectrum). These fits are shown in the top and bottom plots of Figure 8. We ignored the ends of the G230L spectrum and the blue end of the G430L spectrum in these fits, since they tend to be extremely noisy, due to low sensitivity and a high background contribution in these regions, as can be seen in the bottom plot of Figure 8.

In order to determine the contribution of the scattered and stellar components to the continuum at each location, we took advantage of the fact that the flux of the stellar template is essentially zero in the $1400 - 3000 \text{ \AA}$ range. Thus, the contribution of the scattered component at each location is given by the UV flux in this wavelength region. After subtracting the scattered light component, scaled to match the observed UV flux, the

contribution of the stellar component is then given by the residual flux in the optical. The success of this simple procedure is demonstrated by our fits to positions H and I in Figure 8, and, in general, the two components provided a good match to the observed continuum at all locations. The discrepancies between observed and model continuum shapes are small, and may be the result of slight variations in the reddening along the slit. We conclude that the extended continuum is well represented by a combination of scattered and stellar components, whose relative contributions vary as a function of position.

Using the above procedure, we derived brightness profiles along the slit for the scattered and stellar components at 5500 Å; these profiles are plotted in Figure 9. The scattered light is heavily concentrated towards the hot spot, but also shows an extended component over the $-6''$ (NE) to $+2''$ (SW) range. The scattered light is much stronger in the region NE of the hot spot, including a large bump from $-2''.2$ to $-0''.4$. There are also discrete sources of scattered light in addition to the hot spot; the most prominent of these are at positions H and I. These features can also be seen in our far-UV spectrum (Figure 3), since the UV is dominated by scattered light.

In Figure 10, we plot the brightness profiles of the scattering continuum and the [O III] flux along the slit, normalized to their maximum values. The discrete structures in these profiles, represented by the peaks, coincide, although the amplitudes differ. In particular, emission-line knots B (in the red wing of C), H, and I correspond to peaks in the scattered light profile, and knots C and D correspond to the bump in the wing of the scattered light profile. This indicates that regions of ionized gas responsible for the emission lines are approximately co-located with regions responsible for the enhanced electron scattering, although they are not necessarily identical.

The brightness profile of the stellar component in Figure 9 is smoother and less concentrated than that of the scattered component. In addition to a uniform stellar flux

over this region, there is a large bump within $\pm 2''$ the hot spot, which is stronger to the NW; the derived peak of the stellar flux is at $+0''.2$. Since the optical continuum receives a large contribution from the stellar flux, these features can also be seen in the optical spectrum in Figure 4. Our assumption that the spectrum of the hot spot is entirely due to scattered light precludes an accurate determination of the stellar contribution at this location. However, we note that the centroid of the stellar profile is $\sim 0''.3$ NW of the hot spot (close to the observed peak), and it is therefore likely that the stellar flux at the hot spot is less than the peak. At 5500 \AA the total continuum flux at the hot spot is $6.5 \times 10^{-16} \text{ ergs s}^{-1} \text{ cm}^{-2} \text{ \AA}^{-1}$, and the stellar flux is $< 2.0 \times 10^{-16} \text{ ergs s}^{-1} \text{ cm}^{-2} \text{ \AA}^{-1}$, so the contribution of the stellar flux to the hot spot is therefore $< 31\%$. This conclusion is consistent with Antonucci et al.’s (1994) finding that the continuum and broad-line polarizations are the same in small apertures ($0''.3 - 4''.3 \times 1''.4$) centered on the hot spot, indicating the lack of significant dilution of the continuum by starlight.

Figure 11 shows expanded views of the host galaxy spectrum from the bottom plot in Figure 8. The weakness of the UV flux in this spectrum indicates the absence of a significant population of hot young stars. To estimate the age of the population, we used the stellar population models and synthetic spectra developed by Bruzual & Charlot (1993). Figure 11 reveals that a reasonably good match is obtained with a Salpeter initial mass function (IMF), a mass range of $0.1 - 125 M_{\odot}$ and an instantaneous starburst with an age of 2 Gyr. An age ≥ 3 Gyr provides a better match for the flat continuum in the $8000 - 10,000 \text{ \AA}$ region, but a slightly worse fit (lower flux) in the $3000 - 5000 \text{ \AA}$ region. Significantly smaller ages (i.e., ≤ 1.5 Gyr) produce too much flux in the $3000 - 5000 \text{ \AA}$ region and much steeper continua in the $7000 - 10000 \text{ \AA}$ band. Changes in the synthetic spectra are subtle for greater ages or lower mass cutoffs. Given the noisiness of the observed spectra and the reasonably good fits in Figure 11, we place a conservative lower limit of 2 Gyr on the age of this stellar population.

There is a small amount of UV flux in Figure 11 that cannot be explained by this model. This feature does not resemble the smooth “UV upturn” seen in many elliptical galaxies, which starts around 2000 Å and smoothly rises to ~ 1200 Å (and is thought to be due to hot evolved stars, such as extreme horizontal branch stars, see O’Connell 1999). Other explanations for the small UV excess include a minority population of young stars or a small amount of scattered light from the hidden nucleus. However, our main conclusion is still valid: the stellar light is dominated by a old stellar population with an age ≥ 2 Gyr.

4. Discussion and Summary

Our detection of the little blue bump and broad emission lines in the spectrum of the hot spot proves that this compact region is a strong source of reflected radiation from the hidden nucleus, in agreement with the conclusions of Antonucci et al. (1994). The velocity widths of the broad components are not a problem for this conclusion: our FWHM of broad $H\beta$ is substantially larger than the measurement of Caganoff et al. (1991), and the same (to within the errors) as that reported by Miller et al. (1991) for the nucleus. The FWHM of C IV is larger than that of $H\beta$ by ~ 1400 km s $^{-1}$, which is a common occurrence in Seyfert 1 galaxies (Corbin & Boroson 1996). We confirm Caganoff et al.’s measurement of a small equivalent width for $H\beta$, and attribute it to an actual variation of equivalent width (relative to the nonstellar continuum) with aperture size, indicating a decrease in the equivalent width over time. The small equivalent widths of the C IV line and the little blue bump, compared to typical Seyfert 1 galaxies, are additional indications of intrinsically weak broad emission reflected by the hot spot.

The shape of the hot spot’s UV to near-IR continuum is similar to that of Seyfert 1 galaxies, which suggests that we are seeing the intrinsic shape of the continuum, and indicates that 1) the continuum of the hot spot is dominated by scattered light, since a

large stellar contribution would significantly redden the spectrum, and 2) the reflection that we see is due to electron scattering, since dust scattering would “bluen” the spectrum. We estimate that the scattered light contributes more than 69% of the hot spot’s continuum.

We have decomposed the extended continuum emission in the NLR into two components: scattered light and stellar light from the host galaxy. The scattered light contributes essentially all of the UV continuum, and is enhanced in regions of line emission. This explains why the FOC UV images of Macchetto et al. (1994) strongly resemble those in the light of [O III]. It is also consistent with Capetti et al.’s (1995) finding that the UV light must be due to scattering, since it is highly polarized (20 – 65%) over the entire region. In order to determine the total contribution of the hot spot to the scattered light, we retrieved Macchetto et al.’s (1994) UV continuum image centered on 3520 Å. From this image, we find that the hot spot accounts for 20% of the UV flux, and therefore 20% of the scattered light in the inner 500 pc.

We have determined that the continuum of the host galaxy in a region 3'' – 6'' SW of the hot spot is dominated by an old ($\geq 2 \times 10^9$ years) stellar population. We have also confirmed the Lynds et al.’s (1991) suggestion that the high-contrast structure surrounding the nucleus (Figure 2) is stellar. Although the morphology of this structure (Figure 2) is somewhat peculiar, its high contrast indicates that it is a stellar cluster. Our ability to match the continuum in this region with a combination of the scattered light and stellar light further out in the galaxy indicates that it is an old cluster, with an age that is similar to that derived above. Additional evidence for the lack of young stars in this cluster is the absence of this structure in the UV images (Macchetto et al. 1994), and the absence of stellar features in our UV spectra. Thatte et al. (1997) have detected this nuclear stellar cluster from stellar CO features in the H and K bands. Their estimate of its size (FWHM ≈ 50 pc) is consistent with the width of the stellar light profile in Figure 9 (FWHM ≈ 60

pc). Thatte et al. estimate the age of the cluster to be $5 - 16 \times 10^8$ years, which is slightly less than our estimate for the region further out, but consistent with our statements that the cluster and surrounding region are dominated by old stellar populations.

Finally, there is no evidence for another continuum component in our data, which agrees with Antonucci et al.'s (1994) conclusion that there is no additional “featureless continuum” in the nuclear region of NGC 1068. Tran (1995) concludes that a featureless continuum (other than the scattering component) is present in a number of Seyfert 2 galaxies, and Heckman et al. (1995, 1997) indicate that this feature is probably due to hot stars from recent nuclear starbursts. In NGC 1068, however, the closest starburst to the nucleus is at a distance of $\sim 10''$ (720 pc), and none of the prominent starbursts (Neff et al. 1994) are in our slit. Thus there is no clear connection between current AGN activity and recent star formation in NGC 1068.

We thank Tom Brown for help on stellar populations and Fred Bruhweiler for useful discussions on the STIS spectra. We acknowledge support from NASA grant NAG 5-4103.

REFERENCES

- Antonucci, R.R.J. 1993, *ARA&A*, 31, 473
- Antonucci, R.R.J., Hurt, T., & Miller, J. 1994, *ApJ*, 430, 210
- Antonucci, R.R.J., & Miller, J.S. 1985, *ApJ*, 297, 621
- Bland-Hawthorn, J., Gallimore, J.F., Tacconi, L.J., Brinks, E., Baum, S.A., Antonucci, R.R.J., & Cecil, G.N. 1997, *Ap&SS*, 248, 9
- Brinks, E., Skillman, E.D., Terlevich, R.J., & Terlevich, E.T. 1997, *Ap&SS*, 248, 23
- Bruzual, G., & Charlot, S. 1993, *ApJ*, 405, 538
- Caganoff, S., Antonucci, R.R.J., Ford, H.C., Kriss, G.A., Hartig, G., Armus, L., Evans, I.N., Rosenblatt, E., Bohlin, R.C., & Kinney, A.L. 1991, *ApJ*, 377, L9
- Capetti, A., Macchetto, F., Axon, D.J., Sparks, W.B., and Boksenberg, A. 1995, *ApJ*, 452, L87
- Code, A.D., et al. 1993, *ApJ*, 403, L63
- Corbin, M.R., & Boroson, T.A. 1996, *ApJS*, 107, 69
- Evans, I.N., Ford, H.C., Kinney, A.L., Antonucci, R.R.J., Armus, L., & Caganoff, S. 1991, *ApJ*, 369, L27
- Gallimore, J.F., & Tacconi, L.J. 1997, *Ap&SS*, 248
- Heckman, T.M., et al. 1995, *ApJ*, 452, 549
- Heckman, T.M., Gonzalez-Delgado, R., Leitherer, C. Meurer, G.R., Krolik, J., Wilsons, A.S., Koratkar, A., & Kinney, A. 1997, *ApJ*, 482, 114
- Kimble, R.A., et al. 1998, *ApJ*, 492, L83
- Kinney, A.L., Rivolo, A.R., & Koratkar, A.P. 1990, *ApJ*, 357, 338
- Koski, A.T. 1978, *ApJ*, 223, 56

- Kraemer, S.B., Ruiz, J.R., & Crenshaw, D.M. 1998, *ApJ*, 508, 232
- Kriss, G.A., Davidsen, A.F., Blair, W.P., Ferguson, H.C., & Long, K. 1992, *ApJ*, 394, L37
- Kriss G., et al. 1993, in Proc. 8th IAP Mtg. First Light in the Universe: Stars or QSO's, eds. B. Rocca-Volmerange, B. Guideroni, M. Dennefeld, & J. Tran Thanh Van, (Editions Frontieres: Paris), p. 379
- Lynds, R., et al. 1991, *ApJ*, 369, L31
- Macchetto, F., Capetti, A., Sparks, W.B., Axon, D.J., and Boksenberg, A. 1994, *ApJ*, 435, L15
- Miller, J.S., Goodrich, R.W., & Mathews, W.G. 1991, *ApJ*, 378, 47
- Neff, S.G., et al. 1994, *ApJ*, 430, 545
- Nelson, C.H., Weistrop, D., Hutchings, J.B., Crenshaw, D.M., Gull, T.R., Kaiser, M.E., Kraemer, S.B., & Lindler, D. 1999, *ApJ*, submitted
- O'Connell, R.W. 1999, *ARA&A*, in press
- Pogge, R.W. 1988, *ApJ*, 328, 519
- Savage, B.D., & Mathis, J.S. 1979, *ARA&A*, 17, 73
- Snijders, M.A.J., Netzer, H., & Boksenberg, A. 1986, *MNRAS*, 222, 549
- Thatte, N., Genzel, R., Kroker, H., Krabbe, A., Tacconi-Garman, L.E., Maiolino, R., & Tecza, M. 1997, *Ap&SS*, 248, 225
- Tran, H.D. 1995, *ApJ*, 490, 597
- Wills, B.J., Netzer, H., & Wills, D. 1985, *ApJ*, 288, 94

Fig. 1.— Slit Position for the low-dispersion spectra in this paper, at $PA = 202^\circ$, superimposed on an FOC [O III] image (the regular pattern of white marks are reseaux). Bins ($0''.2 \times 0''.1$) used for the extraction of spectra are also plotted. North is up and east is to the left.

Fig. 2.— Slit Position superimposed on a continuum WFPC2 image (centered at 5470\AA). The spatial scale and orientation are the same as in Figure 1.

Fig. 3.— G140L long-slit image of NGC 1068 at $PA = 202^\circ$; wavelength increases to the right and SW is at the top of the image. The locations of emission knots H and I are noted.

Fig. 4.— G430L long-slit image of NGC 1068 at $PA = 202^\circ$; wavelength increases to the right and SW is at the top of the image. The spatial scale is compressed by a factor of $1/2$ compared to Figure 3, due to the larger plate scale for the CCD detector. The locations of emission knots H and I are noted. (The vertical lines are bad CCD columns.)

Fig. 5.— Comparison of continuum spectrum of the NGC 1068 hot spot (smoothed with a 3-point boxcar) with that of the nucleus of NGC 4151 (which has been scaled down in flux by a factor of 0.015).

Fig. 6.— Far-UV spectrum of the NGC 1068 hot spot (smoothed with a 3-point boxcar). Note the broad components of $L\alpha$ and C IV $\lambda 1550$.

Fig. 7.— Spectrum of hot spot in the region of $H\beta$ (upper: observed, lower: narrow $H\beta$ removed).

Fig. 8.— UV to near-IR spectra at four positions along the slit (smoothed with a 5-point boxcar): the hot spot, location H ($-1''.5$ to $-1''.7$), location I ($+1''.3$ to $+1''.5$), and the galaxy ($+3''.0$ to $+6''.0$). Continuum fits are shown (solid: total, dashed: scattered component, dotted: stellar component).

Fig. 9.— Brightness profiles of the scattered and stellar continuum components along the slit. Negative positions correspond to the NE direction.

Fig. 10.— Relative brightness profiles of the scattered continuum and [O III] emission along the slit. Negative positions correspond to the NE direction.

Fig. 11.— Comparison of host galaxy spectrum (dotted line, smoothed with a 5-point boxcar) with synthesized spectra from stellar population models, characterized by instantaneous starbursts that occurred 2 Gyr (solid line) and 3 Gyr (dashed line) ago.

Table 1. STIS Long-Slit Spectra at PA = 202°

Grating	Detector	Coverage (Å)	Exposure (sec)
G140L	far-UV MAMA	1150 – 1724	4736
G230L	near-UV MAMA	1592 – 3176	2280
G430L	CCD	2905 – 5715	540
G750L	CCD	5273 – 10,268	540

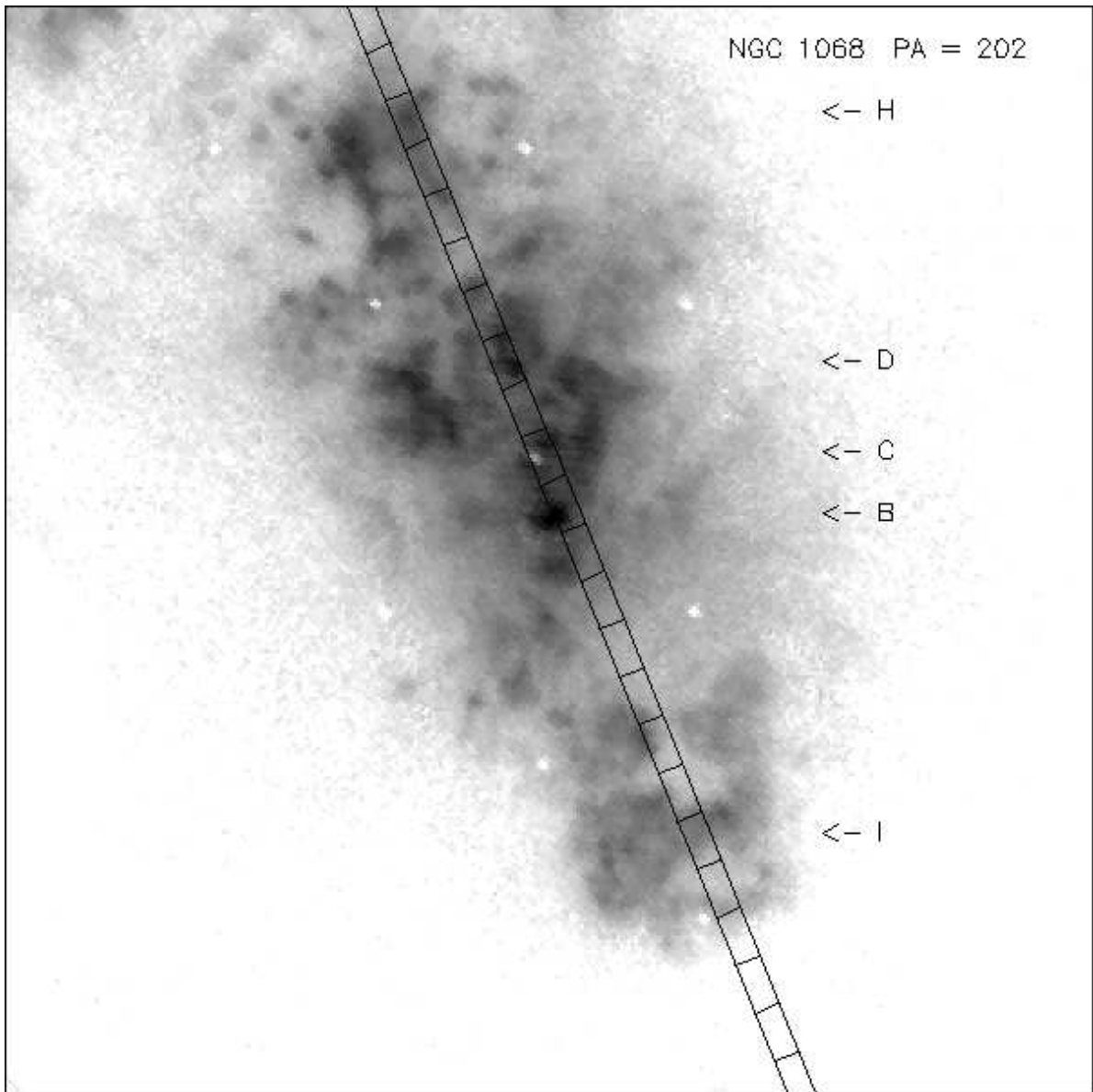


Fig. 1.

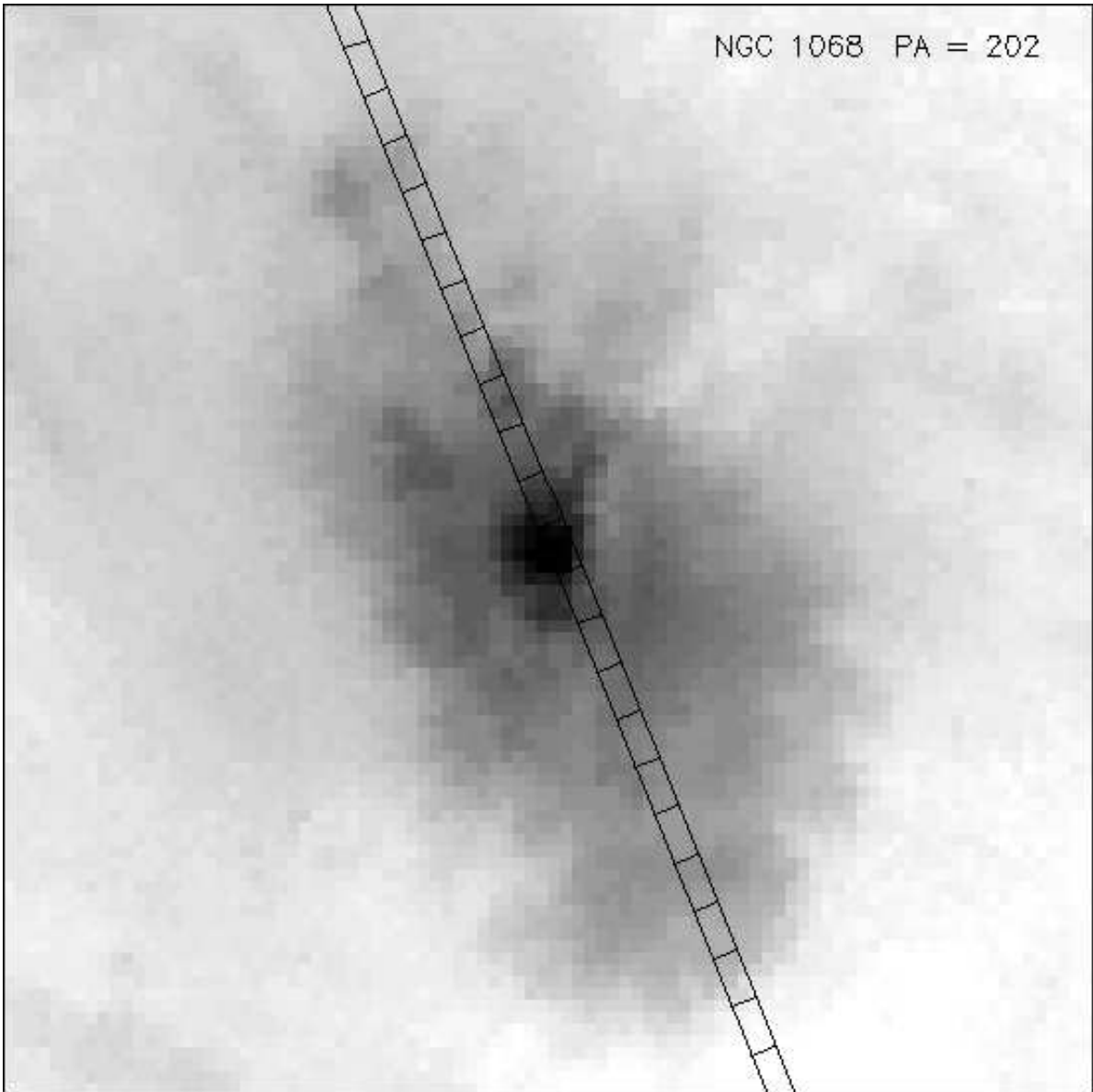


Fig. 2.

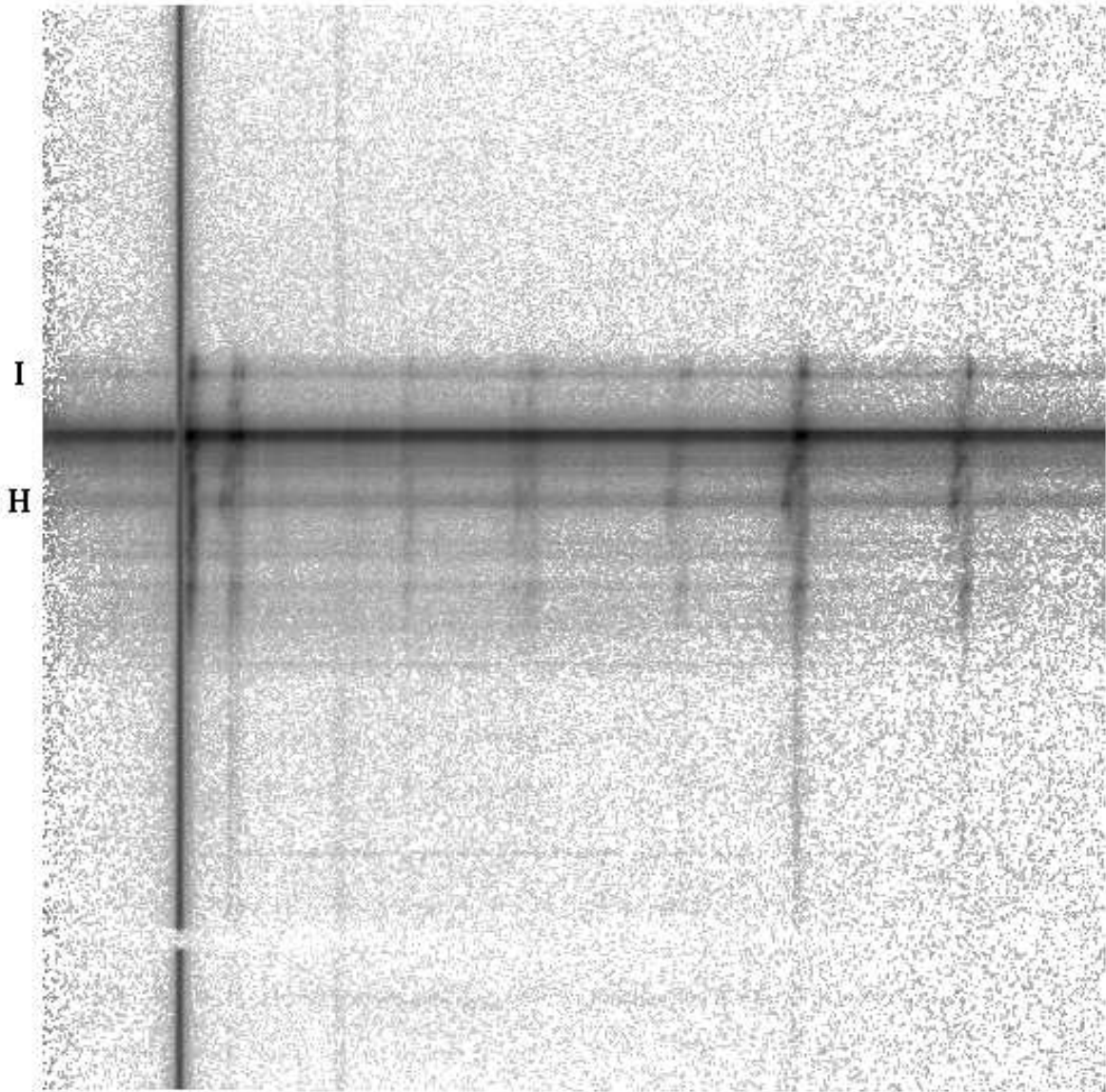


Fig. 3.

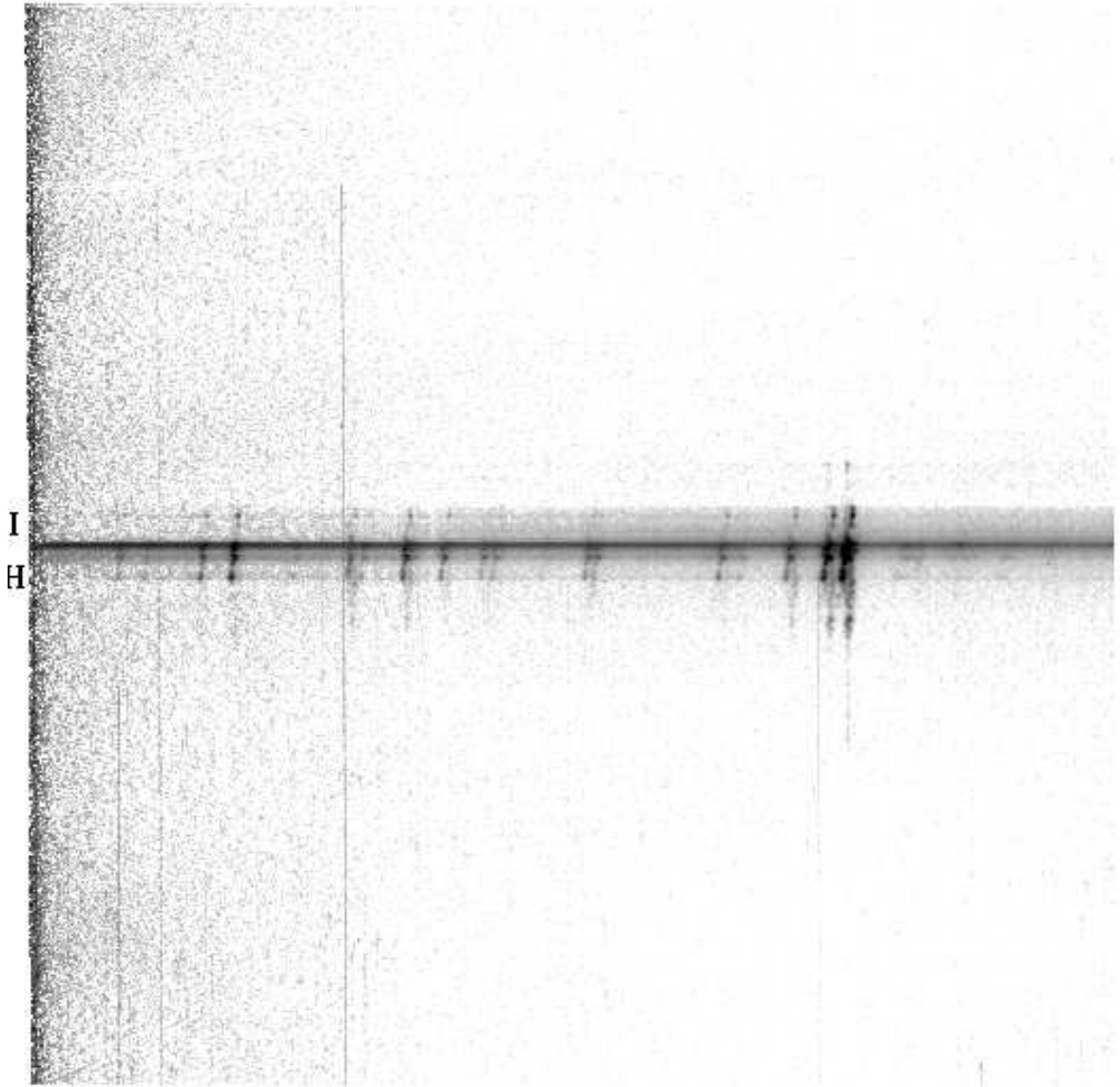


Fig. 4.

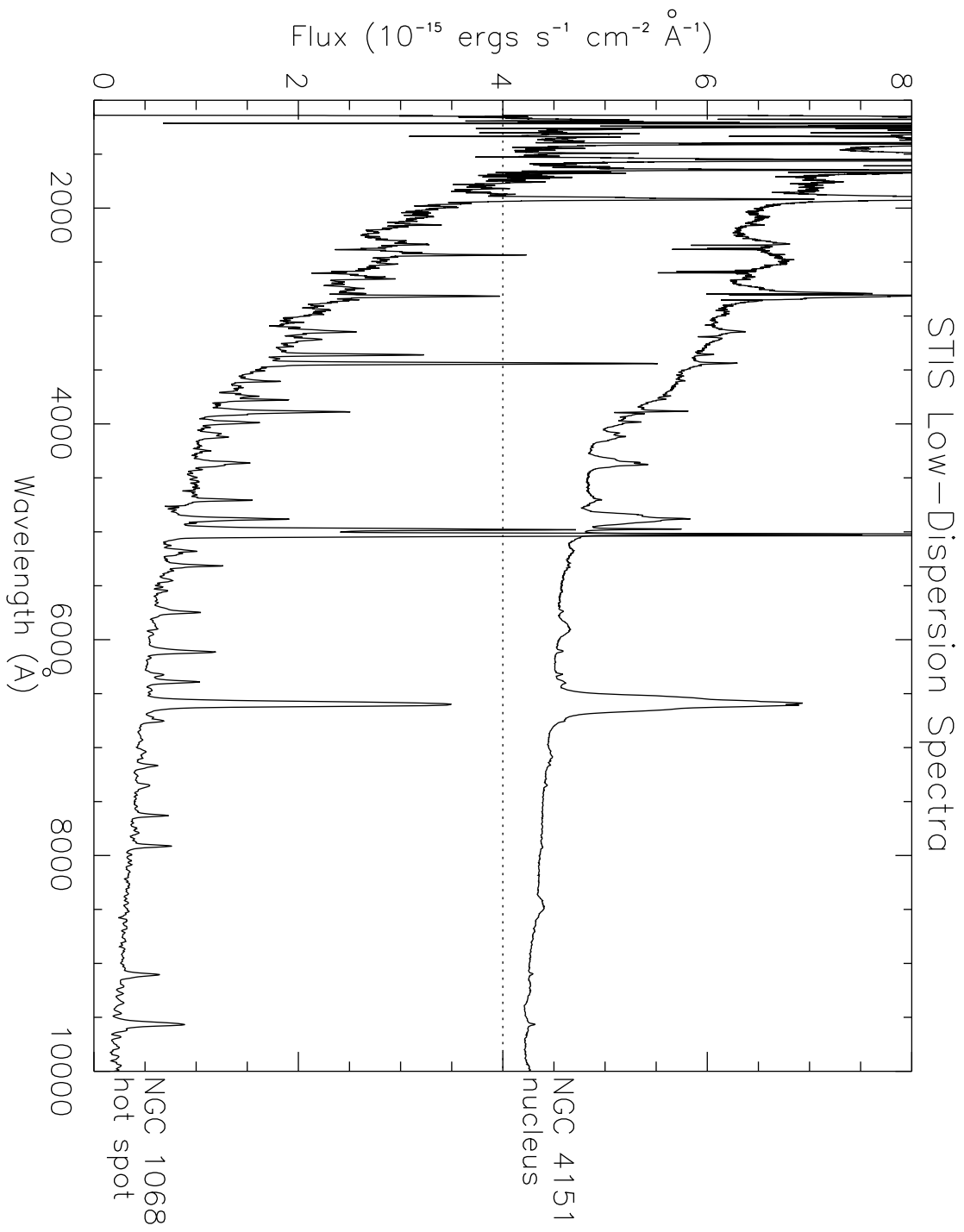


Fig. 5.

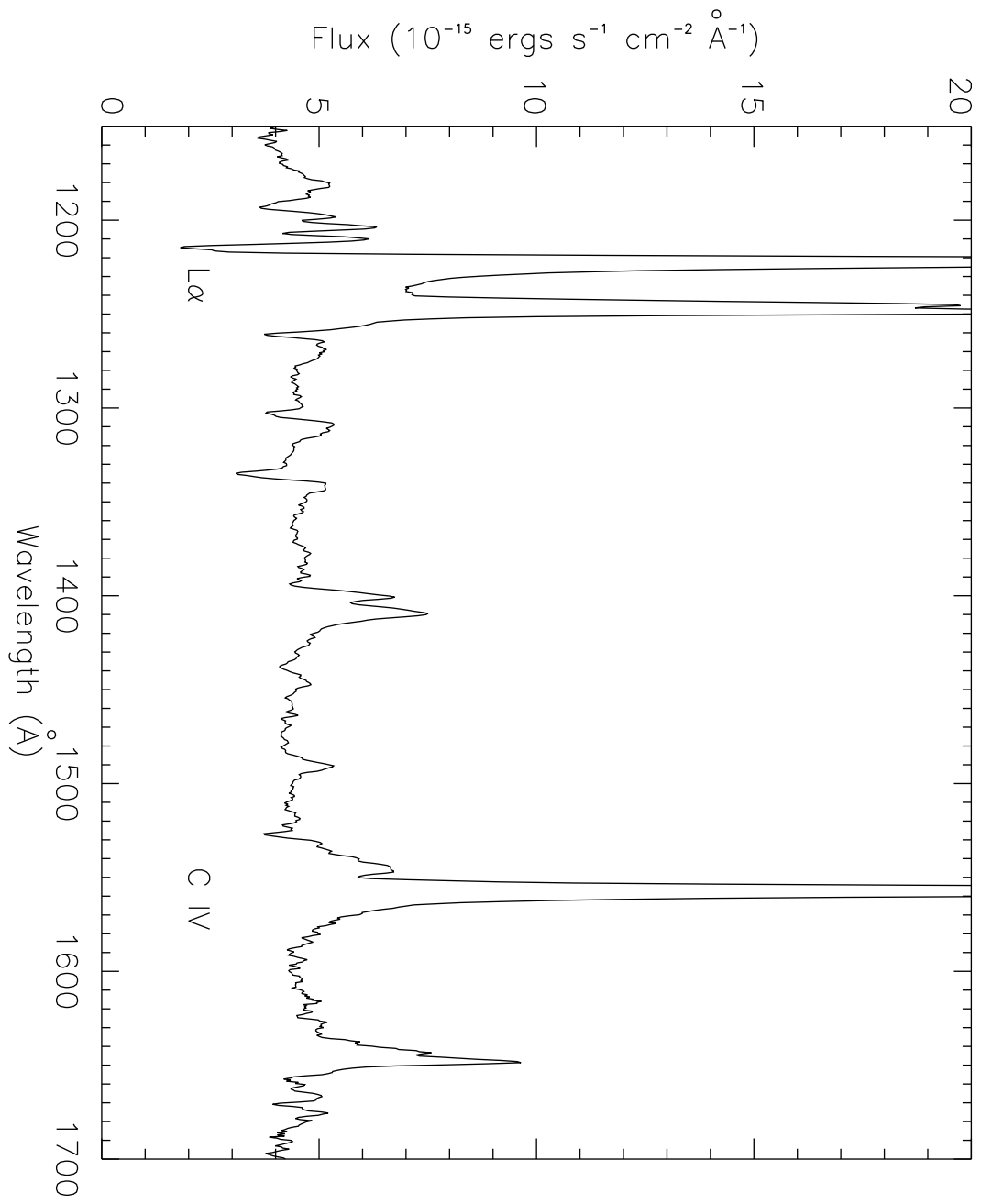


Fig. 6.

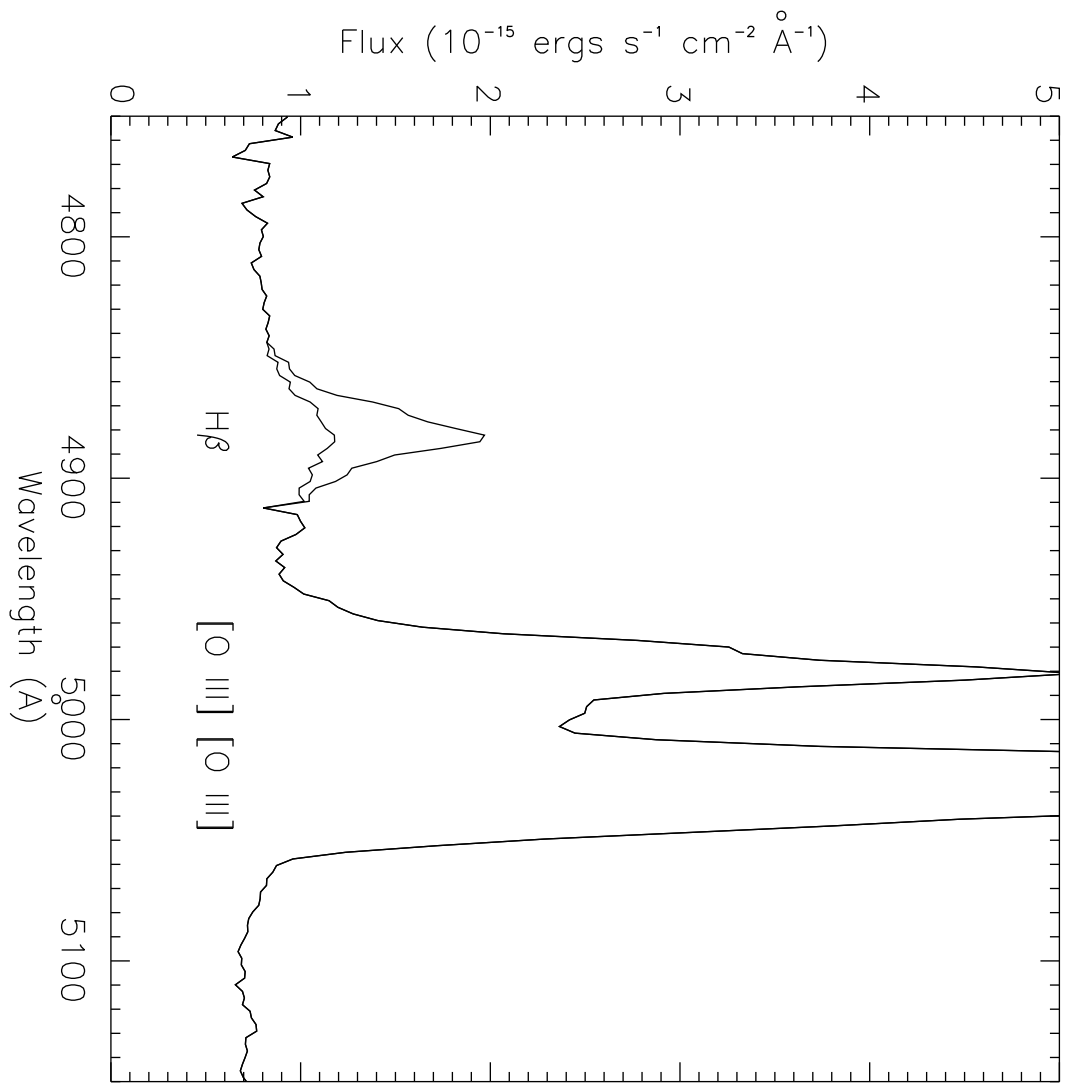


Fig. 7.

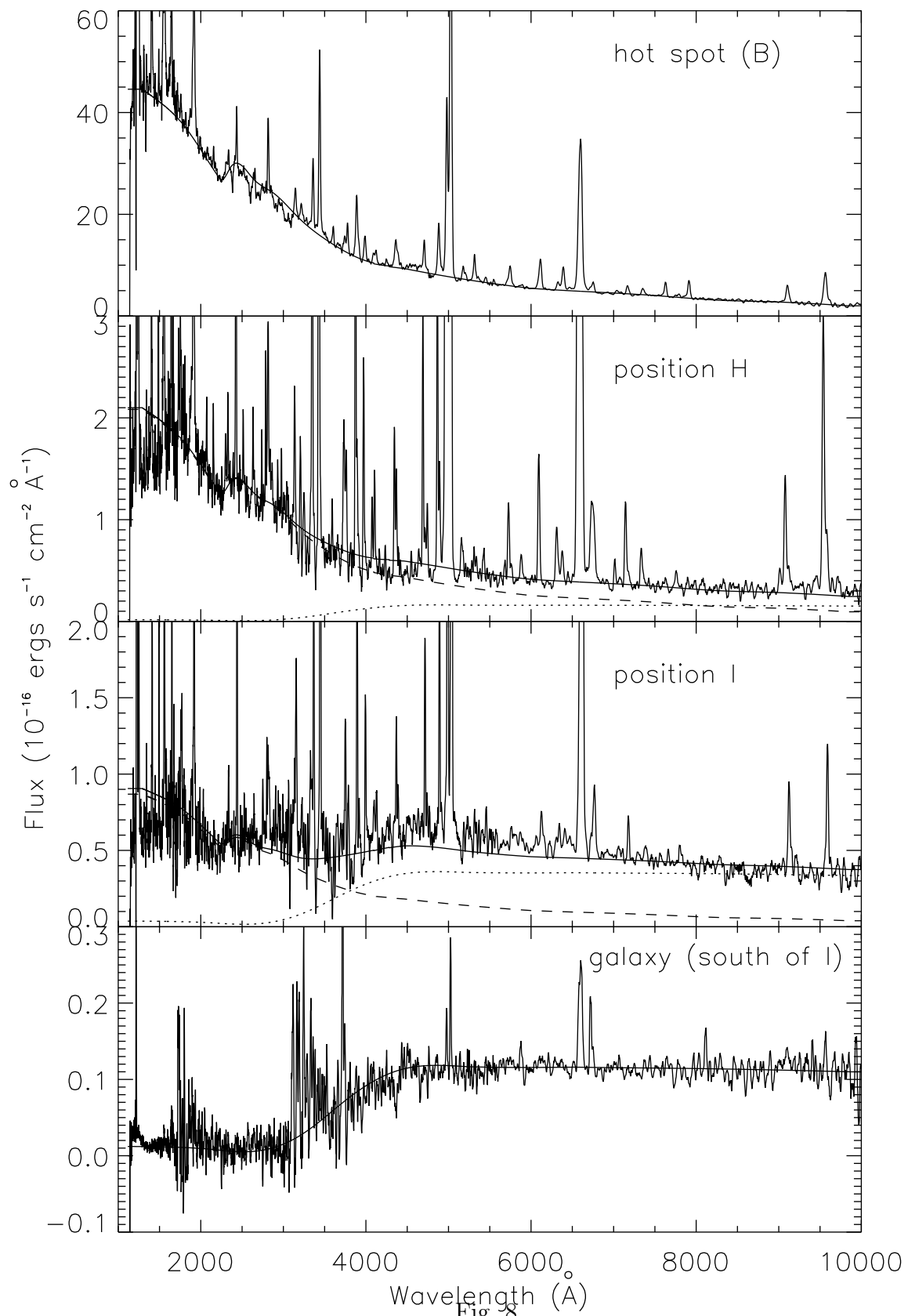


Fig. 8.

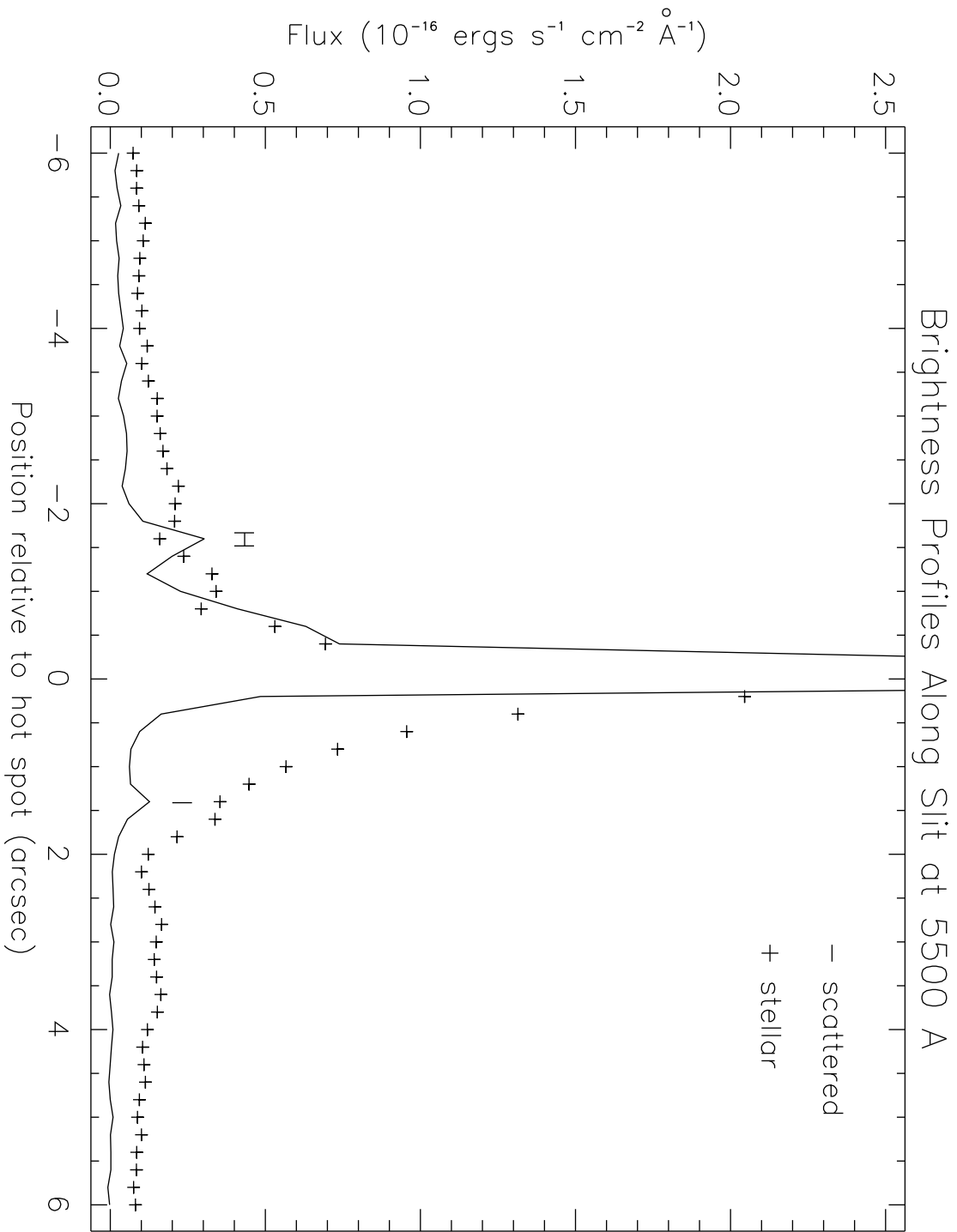


Fig. 9.

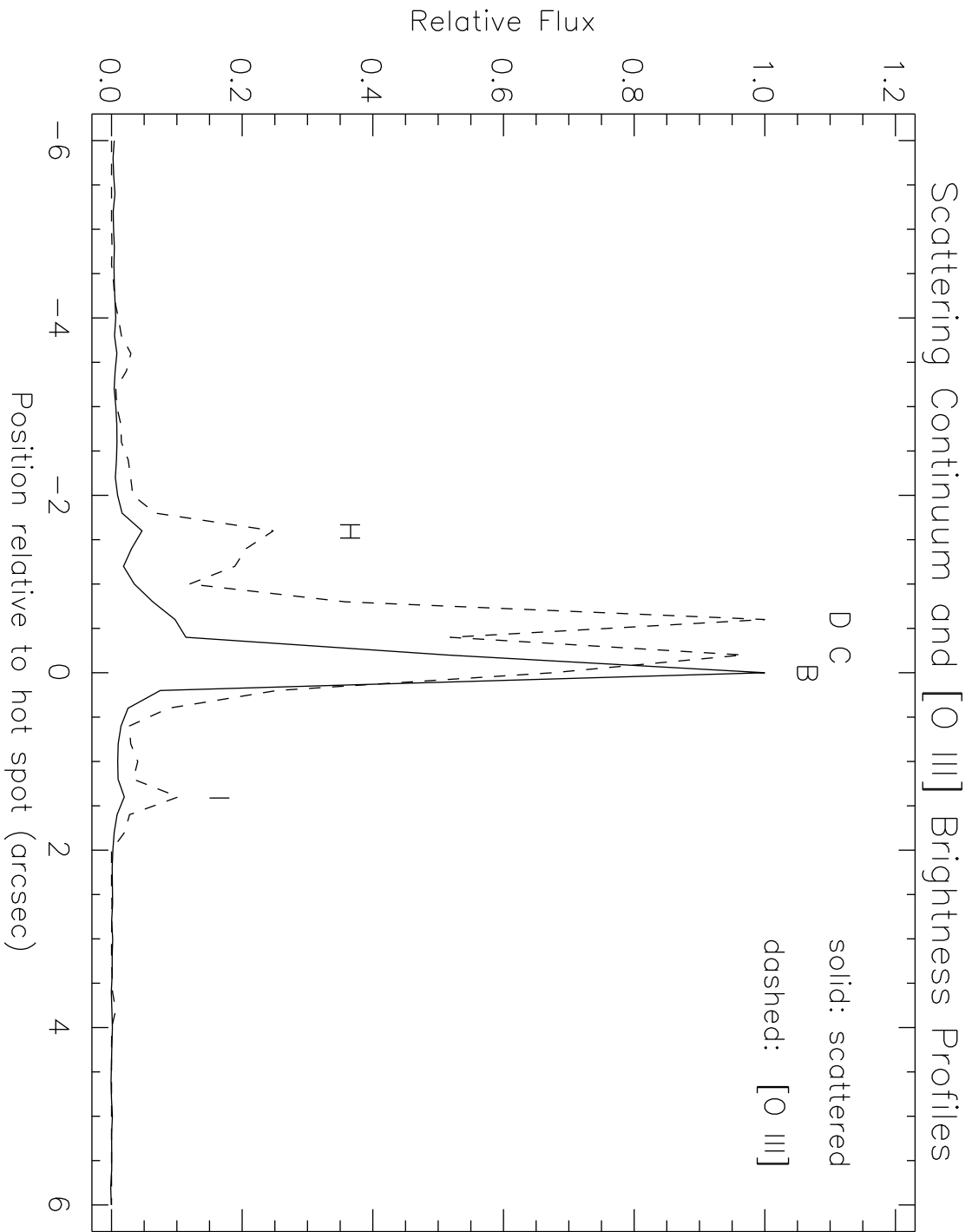


Fig. 10.

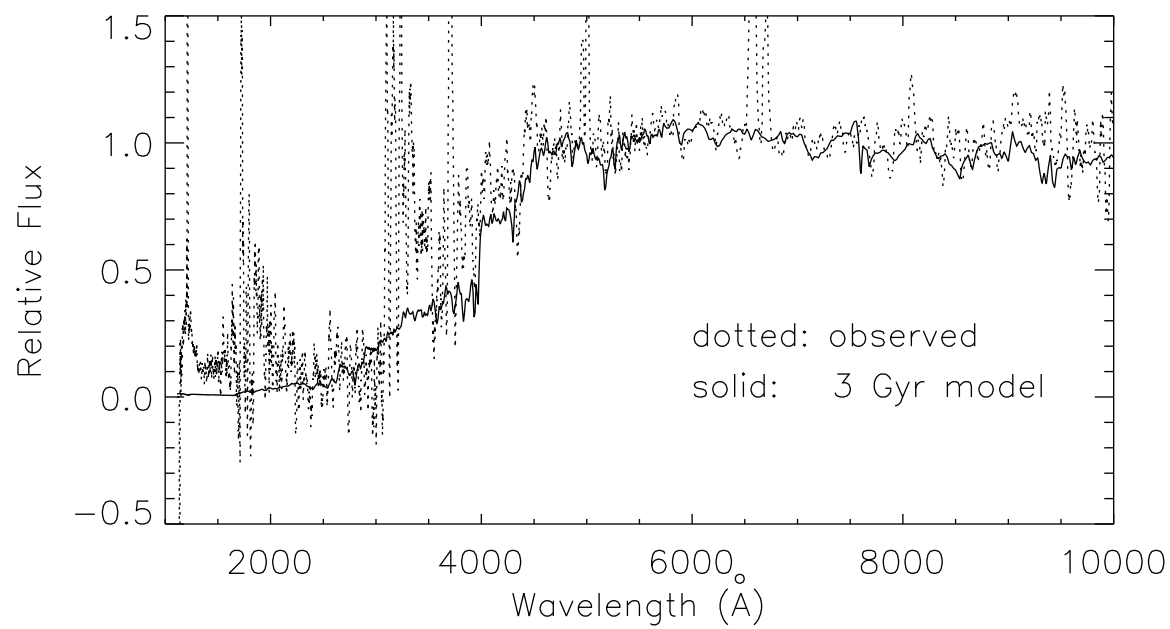
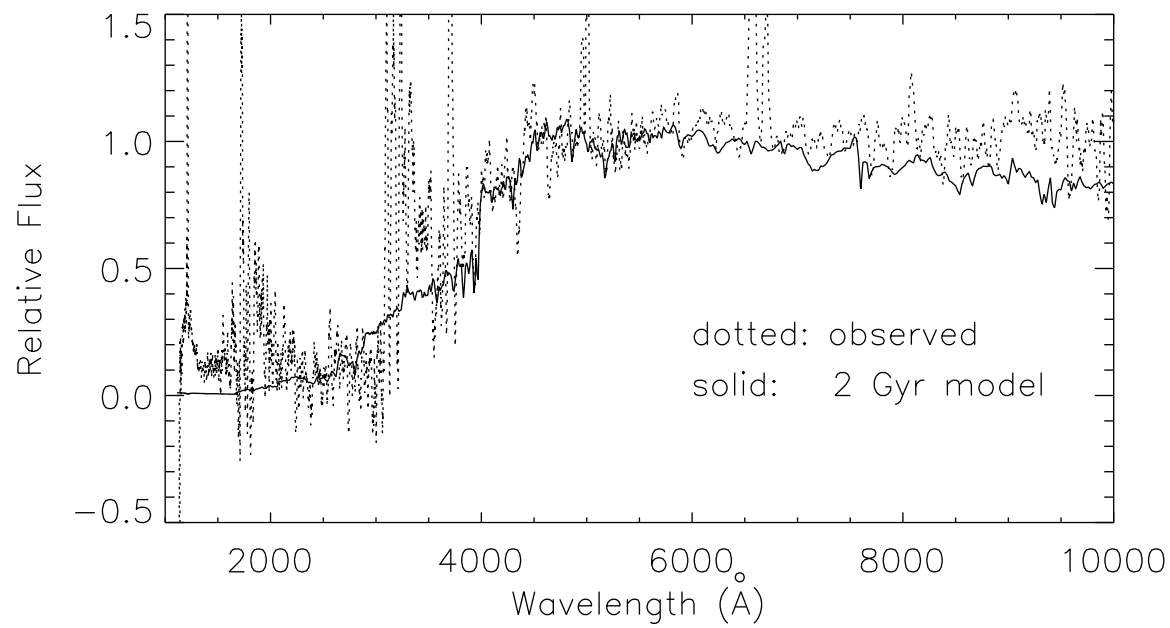


Fig. 11.